JACS
JOURNAL OF THE AMERICAN CHEMICAL SOCIETY
pubs.acs.org/JACS
Article

# Coherent Vibronic Wavepackets Show Structure-Directed Charge Flow in Host–Guest Donor–Acceptor Complexes

Taeyeon Kim,[⊥] Yuanning Feng,[⊥] James P. O'Connor, J. Fraser Stoddart,* Ryan M. Young,* and Michael R. Wasielewski*

Cite This: J. Am. Chem. Soc. 2023, 145, 8389–8400
Read Online
ACCESS | Metrics & More | Article Recommendations | Supporting Information

**ABSTRACT:** Designing and controlling charge transfer (CT) pathways in organic semiconductors are important for solar energy applications. To be useful, a photogenerated, Coulombically bound CT exciton must further separate into free charge carriers; direct observations of the detailed CT relaxation pathways, however, are lacking. Here, photoinduced CT and relaxation dynamics in three host–guest complexes, where a perylene (**Per**) electron donor guest is incorporated into two symmetric and one asymmetric extended viologen cyclophane acceptor hosts, are presented. The central ring in the extended viologen is either *p*-phenylene (**ExV**$^{2+}$) or electron-rich 2,5-dimethoxy-*p*-phenylene (**ExMeOV**$^{2+}$), resulting in two symmetric cyclophanes with unsubstituted or methoxy-substituted central rings, **ExBox**$^{4+}$ and **ExMeOBox**$^{4+}$, respectively, and an asymmetric cyclophane with one of the central viologen rings being methoxylated **ExMeOVBox**$^{4+}$. Upon photoexcitation, the asymmetric host–guest **ExMeOVBox**$^{4+}$ ⊃ **Per** complex exhibits directional CT toward the energetically unfavorable methoxylated side due to structural restrictions that facilitate strong interactions between the **Per** donor and the **ExMeOV**$^{2+}$ side. The CT state relaxation pathways are probed using ultrafast optical spectroscopy by focusing on coherent vibronic wavepackets, which are used to identify CT relaxations along charge localization and vibronic decoherence coordinates. Specific low- and high-frequency nuclear motions are direct indicators of a delocalized CT state and the degree of CT character. Our results show that the CT pathway can be controlled by subtle chemical modifications of the acceptor host in addition to illustrating how coherent vibronic wavepackets can be used to probe the nature and time evolution of the CT states.

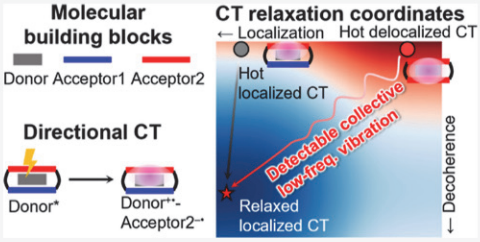




## INTRODUCTION

Light-driven charge transfer (CT) is an essential photophysical process in both natural[1,2] and artificial photosynthesis[3,4] and in organic photovoltaics (OPVs) and other opto-electronics.[5−7] Recent progress in OPVs adopting non-fullerene electron acceptors has seen power conversion efficiencies approach 20%,[8−10] which has re-invigorated interest in this strategy for solar energy conversion. Device performance of OPVs is governed by several steps including light absorption, exciton diffusion to the donor–acceptor interface, formation of a tightly bound CT exciton, charge separation to generate free charge carriers, and diffusion of the charges to an electrode where they are collected. Strong Coulombic interactions in CT excitons impede free carrier generation significantly in OPVs, leading to the formation of relaxed, trapped CT excitons. To overcome the Coulomb barrier and enhance solar cell performance, the CT exciton dynamics need to be better understood.

Two mechanisms to overcome the Coulomb barrier at the molecular scale, delocalization of the initially formed CT state[11−15] and vibronic coupling,[16,17] have been suggested because they can induce rapid charge flow across several adjacent molecules. Charge delocalization plays an essential role in weakening the Coulombic interactions, where only a small amount of delocalization has been observed to impact efficient carrier generation.[18] Vibronic coupling bridges the potential energy surfaces (PESs) along key nuclear coordinates in the sub-picosecond regime, which is a breakdown of the Born–Oppenheimer approximation. Optical pump–probe spectroscopy has been utilized to detect the CT dynamics and characteristic responses in electronic/vibrational signals from local exciton (LE) and CT states.[19−21] In particular, ultrafast broadband transient absorption (BBTA) spectroscopy and two-dimensional electronic spectroscopy (2DES) have been used to detect vibronic wavepackets coupled to the CT reaction coordinate and the degree of charge delocalization.[22−24] Using these tools, we found recently that vibronic coupling effectively drives symmetry-breaking charge separation in a slip-stacked perylenediimide trimer through vibronically mixed Frenkel exciton and CT states.[25,26] Given that this

Received: December 20, 2022
Published: April 5, 2023





https://doi.org/10.1021/jacs.2c13576
J. Am. Chem. Soc. 2023, 145, 8389–8400

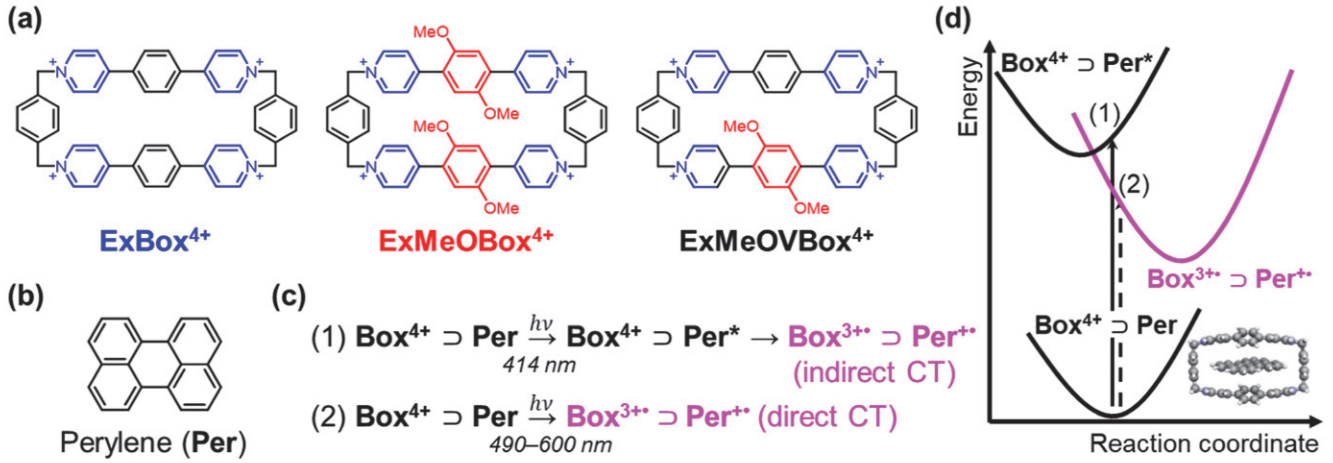


**Figure 1.** Structural formulas of (a) host $\mathbf{Box}^{4+}$ and (b) guest **Per**. (c) Photoinduced dynamics upon (1) photoexcitation of **Per** (indirect CT) and (2) $\mathbf{Box}^{4+} \supset$ **Per** (direct CT). (d) PESs of $\mathbf{Box}^{4+} \supset$ **Per** complexes with LE and CT excitations where the latter has a smaller extinction coefficient compared to the LE state, with a calculated $\mathbf{ExBox}^{4+} \supset$ **Per** complex host–guest structure shown.

**Scheme 1. Syntheses of ExMeOBox·4PF$_6$ and ExMeOVBox·4PF$_6$ Host Molecules**

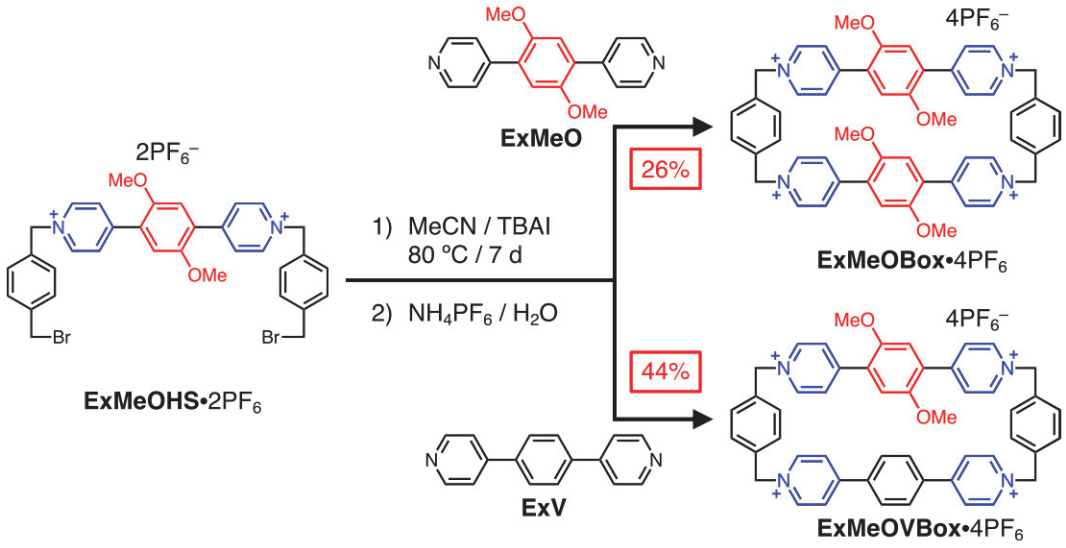


trimer model is symmetric, charge separation can occur in two directions with equal probability.

Directional CT may impact overall power conversion efficiencies in OPVs in comparison to random CT, when donor–acceptor orientations in OPVs are favorable, especially in ternary blends.[27−30] Ultrafast spectroscopy is often used to identify coherent wavepackets at very early times following photoexcitation. However, we have relatively little knowledge about molecular CT excitons themselves and subsequent charge flow from them at early times because most investigations have relied on initial formation of an LE state followed by CT state formation, which, in principle, adds complexity to the interpretation of the signals arising from the LE and CT states. In addition, it is increasingly challenging to discern between spatially delocalized and localized excitons in wavepacket data.

Herein, we address this problem using ultrafast BBTA spectroscopy and 2DES with direct CT state excitation to focus on CT relaxation and coherent vibronic wavepackets of molecular host–guest complexes that can model the noncovalent interactions encountered in OPVs. The host–guest complexes are composed of a perylene (**Per**) electron donor guest (Figure 1a), which is encapsulated in various electron-deficient tetracationic cyclophane ($\mathbf{Box}^{4+}$) hosts (Figure 1b). The central ring in each extended viologen unit is either simple phenylene (black) or electron-rich 2,5-dimethoxyphenylene (red), resulting in three possible combinations. Symmetric boxes with unsubstituted[31] and methoxy-substituted (MeO)[32] central rings are termed $\mathbf{ExBox}^{4+}$ and $\mathbf{ExMeOBox}^{4+}$, respectively, whereas an asymmetric box with one of the central rings at both sides is termed $\mathbf{ExMeOVBox}^{4+}$. Selective photoexcitation of these systems can produce the CT state either through initial formation of the LE state, the indirect mechanism (1), or by direct excitation of the CT state, the direct mechanism (2) (Figure 1c,d). While the LE excitation experiments reveal the directional CT process in the asymmetric complex, the direct CT state excitation experiments using BBTA and 2DES provide characteristic wavepacket signatures of the hot and relaxed CT states and signals from the degree of charge delocalization depending on the symmetry of the hosts.



https://doi.org/10.1021/jacs.2c13576
J. Am. Chem. Soc. 2023, 145, 8389−8400

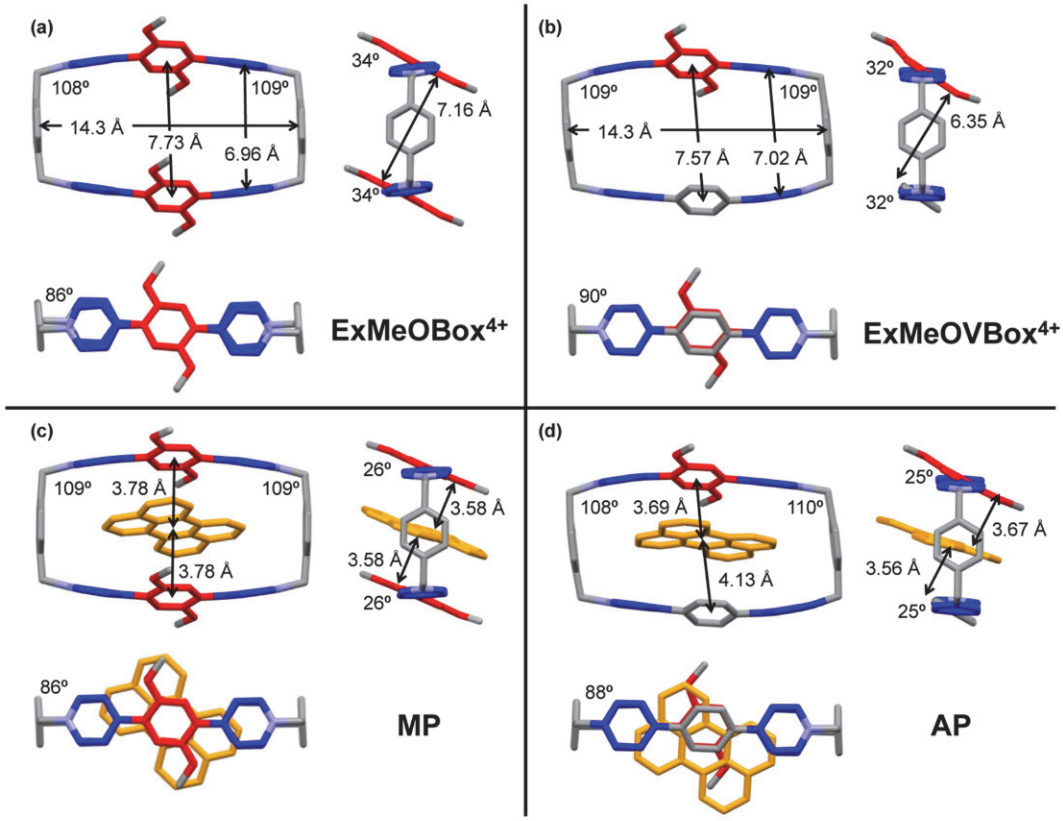


**Figure 2.** X-ray single-crystal (super)structures of (a) **ExMeOBox**$^{4+}$, (b) **ExMeOVBox**$^{4+}$, (c) **MP**, and (d) **AP**.

## RESULTS AND DISCUSSION

**Synthesis.** The synthesis of the symmetric tetracationic cyclophane **ExBox**$^{4+}$ was reported earlier,[31] and the syntheses of MeO symmetric and asymmetric tetracationic cyclophanes **ExMeOBox**$^{4+}$ and **ExMeOVBox**$^{4+}$, respectively, follow similar procedures as shown in Scheme 1. The intermediate **ExMeOHS**·2$PF_6$ was prepared using literature procedures.[32] Briefly, the preparation entails mixing **ExMeOHS**·2$PF_6$ with either **ExMeO** or **ExV** in a ratio of 1:1 in dry MeCN in the presence of ∼20 mol % tetrabutylammonium iodide (TBAI) and heating under reflux. This reaction was followed by the addition of solid tetrabutylammonium chloride (TBAC) to precipitate the crude products. The crude products were subjected to reverse-phase C-18 column chromatography, followed by counterion exchange with an excess of $NH_4PF_6$ in aqueous solution to precipitate the pure products, which were dried in vacuo to obtain **ExMeOBox**·4$PF_6$ and **ExMeOVBox**·4$PF_6$.

**Host−Guest Binding.** The binding constants for the host−guest complexes were determined by $^1$H NMR titration. The binding constant for the complex **ExBox**$^{4+}$ ⊃ **Per** (**EP**), $K_a$ = 8.8 ± 6.7 × 10$^4$ M$^{-1}$, was reported earlier.[31] Here, a solution of either **ExMeOBox**$^{4+}$ or **ExMeOVBox**$^{4+}$ (0.5 mM) in $CD_3CN$ was added to a **Per** solution (2.5 mM), and an $^1$H NMR spectrum was recorded after each addition. The NMR titration data for **ExMeOBox**$^{4+}$ show the formation of the complex **ExMeOBox**$^{4+}$ ⊃ **Per** (**MP**), which is based on the upfield shift of the proton resonances in the host and more significantly the downfield shift of those in the guest **Per** (Figure S1, top). By following the change in chemical shift for the *ortho*-protons in **Per**, a binding isotherm could be determined using a 1:1 receptor−substrate binding model[33] (Figure S1, bottom), yielding an association constant $K_a$ = (4.39 ± 0.19) × 10$^3$ M$^{-1}$. The corresponding data for **ExMeOVBox**$^{4+}$ show the formation of the complex **ExMeOVBox**$^{4+}$ ⊃ **Per** (**AP**), which exhibits similar shifts of its $^1$H NMR resonances during its titration (Figure S2, top), which yields $K_a$ = (5.68 ± 0.15) × 10$^3$ M$^{-1}$ (Figure S2, bottom). The value of $K_a$ for the symmetric complex **MP** is slightly lower than that for the asymmetric **AP**, and they both are one order of magnitude lower[31] than $K_a$ of **ExBox**$^{4+}$ ⊃ **Per** (**EP**), which most likely results from the steric hindrance of the methoxy groups on **ExMeOBox**$^{4+}$ and **ExMeOVBox**$^{4+}$.

**Host−Guest Complex Single Crystal (Super)structures.** The X-ray single-crystal structures of **ExMeOBox**$^{4+}$ (Figure 2a) and **ExMeOVBox**$^{4+}$ (Figure 2b) reveal box-like cavities, measuring 14.3 Å in length and 7.0 and 7.6−7.7 Å in width at their periphery and center, respectively. The two dihedral angles between the adjacent electron-deficient pyridinium and central (dimethoxy)phenylene rings are 34 and 32°, respectively, which are both greater than the average dihedral angle (∼30°) present in **ExBox**$^{4+}$. The extended solid-state superstructures of **ExMeOVBox**$^{4+}$ reveal (Figure S2) that the central rings face each other, with a centroid-to-centroid distance of 3.6 Å and a plane-to-plane distance of 4.6 Å. The overall superstructure of **ExMeOVBox**$^{4+}$ reveals a parallel arrangement of the tetracationic cyclophanes which is similar to that of the published[32] **ExMeOBox**$^{4+}$ superstructure.

In the symmetric host−guest complex **MP** (Figure 2c), the **Per** guest is located parallel to the center of the host cavity, exhibiting the same centroid-to-centroid (∼3.8 Å) and plane-to-plane (∼3.6 Å) distances. In the asymmetric complex **AP** (Figure 2d), however, the **Per** guest experiences unbalanced interactions from the different extended viologen units on each



https://doi.org/10.1021/jacs.2c13576
J. Am. Chem. Soc. 2023, 145, 8389−8400

side, resulting in unequal distances to two central rings and non-parallel, non-centroid stacking in the cavity. Additional (super)structural information on the crystal packing of **ExMeOVBox**$^{4+}$, **MP**, and **AP** is summarized in Figures S3–S5, respectively.

**Energetics.** The one-electron redox potentials of the host molecules **ExBox**$^{4+}$ and **ExMeOBox**$^{4+}$ and the **Per**-containing host–guest molecules **EP**, **AP**, and **MP** in MeCN were determined (Figures S6–S10) using differential pulse voltammetry (DPV) while those of **ExMeOVBox**$^{4+}$ were determined (Table 1) previously.[34] The data for the **Box**$^{4+}$

**Table 1. Summary of Reduction Potentials ($E_{red}$) Obtained from DPV in MeCN (V vs Ag/AgCl)**

| ExBox$^{4+}$ | ExMeOVBox$^{4+}$ | ExMeOBox$^{4+}$ | EP | AP | MP |
|---|---|---|---|---|---|
| −0.72 | −0.76 | −0.80 | −0.77 | −0.83 | −0.82 |

cyclophanes and their host–guest complexes containing **Per** show that the presence of the methoxy groups on the central ring of the extended viologens results in making the viologens more difficult to reduce by about 40–80 mV as was noted earlier.[34] The corresponding oxidation potential of **Per** in **ExBox**$^{4+}$ ⊃ **Per** is 1.16 V vs Ag/AgCl. Given that all of the photophysical experiments presented here are conducted in MeCN, the same high-dielectric constant solvent in which the electrochemistry was performed, the CT state energies can be estimated by simply summing the redox potentials for guest oxidation and host reduction, $\Delta G_{CT} = E_{ox} - E_{red}$, which yields $\Delta G_{CT}$ = 1.93, 1.99, and 1.98 eV for **EP**, **AP**, and **MP**, respectively. See also Table S1. These estimates correlate reasonably well with the observed onset of the CT absorption bands of **EP**, **AP**, and **MP** (Figure 3a), which all occur around 2 eV.

**Steady-State Absorption Spectra.** Steady-state absorption spectra of the three host–guest complexes are shown in Figure 3a. The corresponding spectra of **ExBox**$^{4+}$ and **ExMeOVBox**$^{4+}$ have been reported earlier[31,34] while those of **ExMeOBox**$^{4+}$ are given in Figure S11. The absorption spectra of the complexes have a broad and intense absorption band at 300–320 nm which is primarily attributed to the $\pi$–$\pi^*$ **Box**$^{4+}$ absorption (Figure 3a). Also, three regions where **Per** contributes to the transitions are denoted as i, ii, and iii in the absorption spectra. These transitions are (i) forbidden CT transitions, (ii) weakly allowed hot CT transitions, and (iii) strong LE-like transitions, where the frontier molecular orbitals of **EP** and **AP** contribute most strongly to these transitions.

We computed the optimized singlet ground-state geometry for **EP**, **MP**, and **AP** (Figure 3b,c) and for the reduced box species using time-dependent density functional theory (TD-DFT) at the B3LYP/6-31++G(d) level of theory as described in the Supporting Information. The highest occupied molecular orbitals (HOMOs) and the lowest unoccupied molecular orbitals (LUMOs) and several adjacent orbitals are given in Figure 3d,e. CT bands of organic host–guest complexes are typically weak because through-bond CT interactions are not present.[35] While this observation applies to the forbidden CT transition (region i), the hot CT transitions (region ii) are weakly allowed presumably due to LE and CT state mixing. In this respect, a three-state model describes[35,36] the electronic states of these CT complexes more accurately than the two-state Mulliken–Hush model[37] because the two-state model overestimates the coupling between the

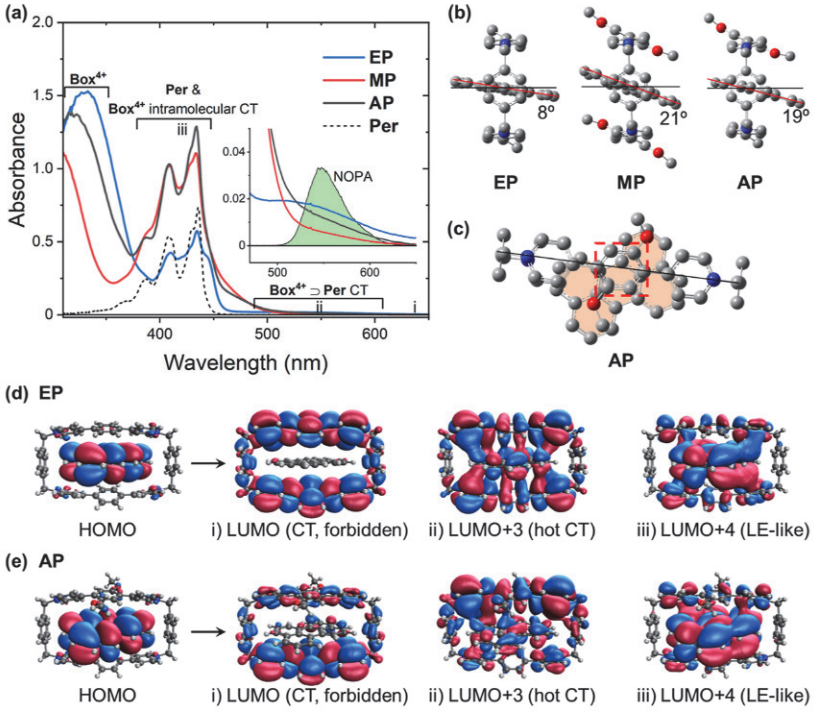


**Figure 3.** (a) Steady-state absorption spectra of the three host–guest complexes (solid lines) and **Per** (dashed line). The inset displays magnified CT bands of the complexes and a NOPA spectrum (green) used for 2DES/BBTA measurements. Labels i, ii, and iii denote the LE-like, hot CT, and forbidden CT transitions, respectively, as shown in (d,e). Optimized structures of the complexes: (b) side views of three complexes with the tilt angle of **Per** to the central plane (black) and (c) top view of **AP**, where the filled color represents **Per** and the red box highlights the location of the core rings. Molecular orbitals of (d) **EP** and (e) **AP** with the strongest contributing transitions.



https://doi.org/10.1021/jacs.2c13576
J. Am. Chem. Soc. 2023, 145, 8389–8400

LE and ground states and does not account for LE and CT state mixing (Figure S13). This mixing is supported by LUMO +4 and LUMO+3 (Figure 3d,e), which possess the highest oscillator strength (Table S2), as the electron density is distributed over both the host and the guest molecules. As a result of this mixing, the LE-like transitions (region iii) are slightly blue-shifted with respect to those of **Per** by ~60 $cm^{-1}$ for **EP** and ~110 $cm^{-1}$ for **MP** and **AP** (Figure S12). Interestingly, the almost identical energy shift for **MP** and **AP** and the similar absorption tail beyond 500 nm can be explained by the torsional angles of the **Per** in the host cavity (21 and 19° for **MP** and **AP**, respectively, Figure 3b), which maximize the orbital overlap (through-space interactions) between the **Per** and the MeO-substituted extended viologen (**ExMeOV**$^{2+}$) unit rather than between the **Per** and the unsubstituted extended viologen (**ExV**$^{2+}$) side. This difference in geometry is ultimately due to the steric hindrance imposed by the MeO groups on the central phenylene ring.

**Photoinduced CT upon LE-like State Excitation.** To examine the photoinduced CT dynamics in the three complexes, we acquired the TA spectra using narrowband excitation at 414 and 500−545 nm that are each resonant with the LE-like and hot CT states, respectively (Figures S14−S18). All of the complexes exhibit rapid CT dynamics (<300 fs) after 414 nm excitation, followed by charge recombination (CR) in $\tau_{CR}$ = 40.3 ± 0.9, 48.6 ± 0.3, and 46.9 ± 0.3 ps for **EP**, **MP**, and **AP**, respectively, where the dynamics of **EP** agree well with the previous report.[38] Absorption spectra of the charged species (**Box**$^{3+\bullet}$ ⊃ **Per**$^{+\bullet}$) and the **Per*** absorption signals are shown in Figure 4a. The **Per**$^{+\bullet}$ absorption band is located at 530−540 nm,[38,39] while the **Box**$^{3+\bullet}$ radical ions show distinctive absorption bands in both the visible and near-infrared regions. Compared to the previously reported **ExBox**$^{3+\bullet}$ absorption bands at ~500 and ~1175 nm, **ExMeOBox**$^{3+\bullet}$ (**ExMeOVBox**$^{3+\bullet}$) absorption bands are located at ~537(534) and ~1150(1157) nm. The similar spectral signatures of **ExMeOBox**$^{3+\bullet}$ and **ExMeOVBox**$^{3+\bullet}$ and their similar CR time constants indicate that the photoinduced CT process in **AP** reduces the **ExMeOV**$^{2+}$ unit preferentially.

It is worth noting that the photoinduced CT pathway of **AP** is thermodynamically uphill, as the reduction potential of **ExMeOV**$^{2+}$ is 40−80 mV more negative than that of **ExV**$^{2+}$ as confirmed by electrochemistry measurements on the complexes containing **Per** (Table 1). This unexpected outcome most likely results from the biased **Per** orientation that enforces stronger through-space interactions and thus stronger donor−acceptor electronic coupling and a faster CT rate with the **ExMeOV**$^{2+}$ side. This effect combined with the short CT lifetimes (<50 ps) prevents a second CT from the **ExMeOV**$^{+\bullet}$ to the **ExV**$^{2+}$ unit from occurring. The CR dynamics suggest that the back electron transfer of these complexes is in the Marcus inverted region.[40,41] The slight differences between **MP** and **AP** in the CR time constants and spectral features could result from subtle differences in the orientation and location of the **Per** inside the host cavity (Figure 3b,c) which enhance the through-space interaction between the **Per** and the **ExMeOV**$^{2+}$ unit.

**Photoinduced CT upon Direct CT Excitation.** When the CT state is excited directly, CT bands are observed immediately (Figures 4a and S19). Note that all time-resolved CT excitation experiments were performed with ca. 0.1 absorbance at the CT bands. Two important advantages of direct CT excitation are the following: (1) The observed signals are free from those of the LE-like state, including those of unbound **Per**, which enables detailed analysis. (2) Relaxation processes in the CT state can be understood in terms of the degree of charge delocalization and the degree of mixing between the LE and CT states by monitoring the characteristic electronic and vibrational signals. Upon broadband excitation using a noncollinear optical parametric amplifier (NOPA) output (inset in Figure 3a), the hot CT state is directly populated followed by relaxation processes where **AP** seems to exhibit a small **ExV**$^{+\bullet}$ absorption unlike the LE-like excitation experiments, which will be clarified by the 2DES experiments described below.

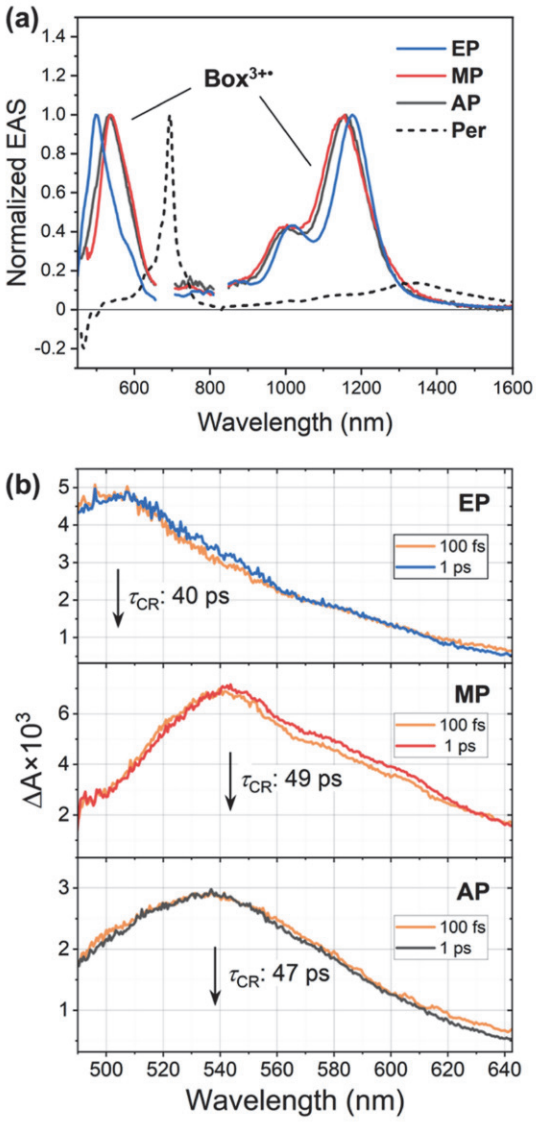


**Figure 4.** (a) CT state absorption from the evolution-associated spectra of the three complexes and **Per** following narrowband excitation. (b) TA spectra comparison between 100 fs and 1 ps for the three complexes using BBTA measurements where CR time constants (back electron transfer) are shown.

Spectral changes between 100 fs and 1 ps are only observed (Figure 4b) in the symmetric complexes, **EP** and **MP**. These spectral changes as a function of time are plotted as a signal ratio ($\rho$) in Figure 5, where $\rho_{505/540} = \Delta A_{505nm}/\Delta A_{540nm}$. Wavelengths/frequencies for signal ratios were selected to reflect their dynamic red shifts compared to the initial band


https://doi.org/10.1021/jacs.2c13576
J. Am. Chem. Soc. 2023, 145, 8389−8400

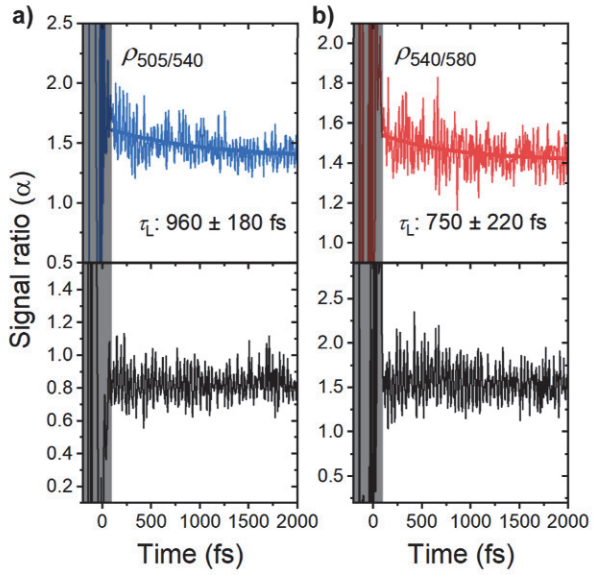


**Figure 5.** Signal ratio ($\rho$) as a function of time from BBTA results. (a) $\rho_{505/540}$ of **EP** (top) and **AP** (bottom) and (b) $\rho_{540/580}$ of **MP** (top) and **AP** (bottom). $\tau_L$ represents the localization time constant. Note that the periodic fluctuations in the signals are due to vibrational coherences rather than noise.

maxima. TD-DFT calculations show that electron density of the hot CT state in the symmetric complexes is distributed (Figures 3d and S20) over both extended viologen units evenly, leading to the delocalized CT state, which has been observed in other molecular systems.[42,43] As a result of fluctuations in host−guest interactions involving solvent−solute reorganization and host vibrations, which can affect the host−guest geometry directly, the delocalized CT state of the $\mathbf{Box}^{3+\bullet}$ hosts localizes onto one of the extended viologen units, which can affect the electronic spectra in terms of a breakdown of the Laporte rule.[44] In this fashion, $\rho$ decreases rapidly with a localization time constant ($\tau_L$) of 960 and 750 fs for **EP** and **MP**, respectively, while **AP** does not display such an evolution in either $\rho_{505/540}$ or $\rho_{540/580}$. This result implies that electronic transitions could capture the localization process in **EP** and **MP**,[45,46] while the relaxation process on the PES of the localized CT state in **AP** is difficult to detect via its electronic transitions.

**Vibronic Wavepackets in the CT States.** Vibrational spectroscopy is a powerful approach to identify photoinduced CT reactions along nuclear coordinates[47−50] and is also capable of detecting the exciton size and location.[51−53] Accordingly, vibronic wavepackets were explored to understand CT state relaxation, and these wavepackets were directly launched on the CT state PES by broadband excitation. We analyzed the coherent oscillations observed in BBTA results by subtracting the population dynamics from the TA signals followed by fast Fourier transformation (FFT). Fourier power spectra of **EP**, **MP**, and **AP** are compared in Figure 6a, where the signals are averaged from 500 to 550 nm to obtain a high signal-to-noise ratio. Note that the analysis is based on the assumption that the wavepacket signals originate from the $\mathbf{Box}^{3+\bullet}$ species owing to (1) the comparatively much broader

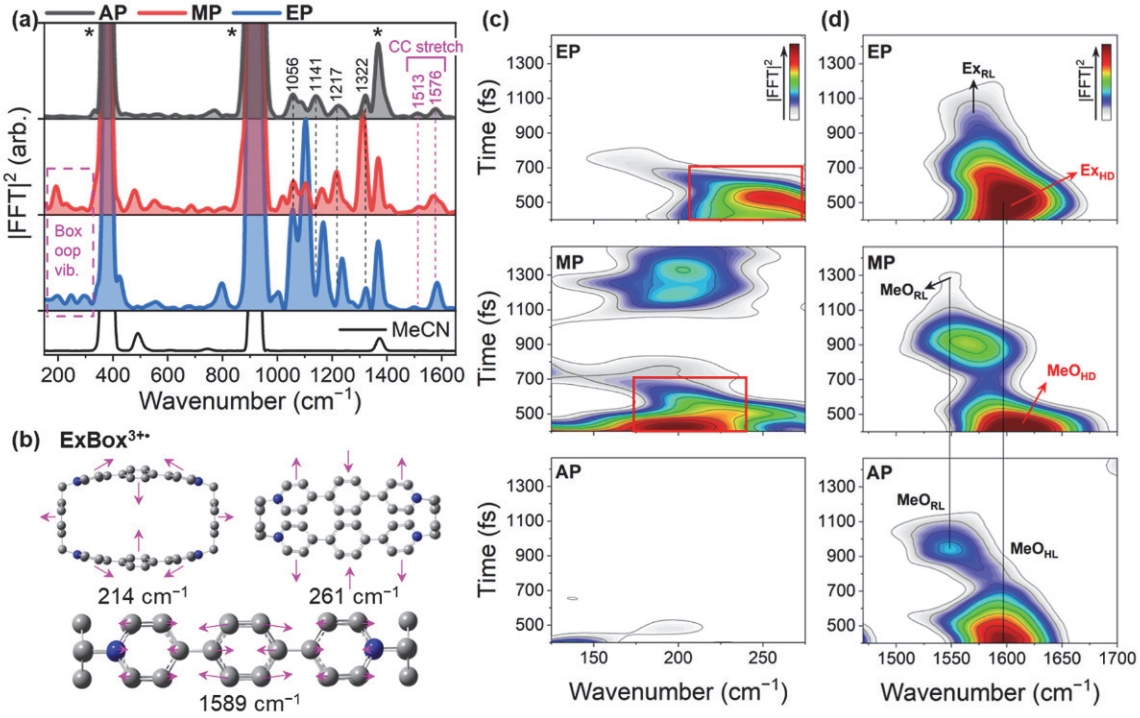


**Figure 6.** (a) Fourier power spectra of the three complexes. MeCN modes are denoted with asterisks. Several out-of-plane modes from symmetric **EP** and **MP** are marked with a dashed box in the low-frequency regions (150−300 $cm^{-1}$), and high-frequency CC stretching modes are marked at 1500−1650 $cm^{-1}$ (magenta) and ring deformation modes at 1000−1350 $cm^{-1}$ (black). (b) Representative low- and high-frequency modes of $\mathbf{ExBox}^{3+\bullet}$ are shown with displacement vectors (arrows). Spectrograms of the three complexes using STFT analysis in (c) low- and (d) high-frequency region. Short-lived low-frequency modes in **EP** and **MP** are marked (red boxes). Ex and MeO refer to $\mathbf{ExBox}^{3+\bullet}$ and $\mathbf{ExMeOBox}^{3+\bullet}$, respectively, and subscripts (RL, HL, and HD) represent relaxed (R), hot (H), delocalized (D), and localized (L). CC stretching frequencies of $MeO_{HL}$ and $MeO_{RL}$ are marked with the vertical lines (black).



https://doi.org/10.1021/jacs.2c13576
J. Am. Chem. Soc. 2023, 145, 8389−8400

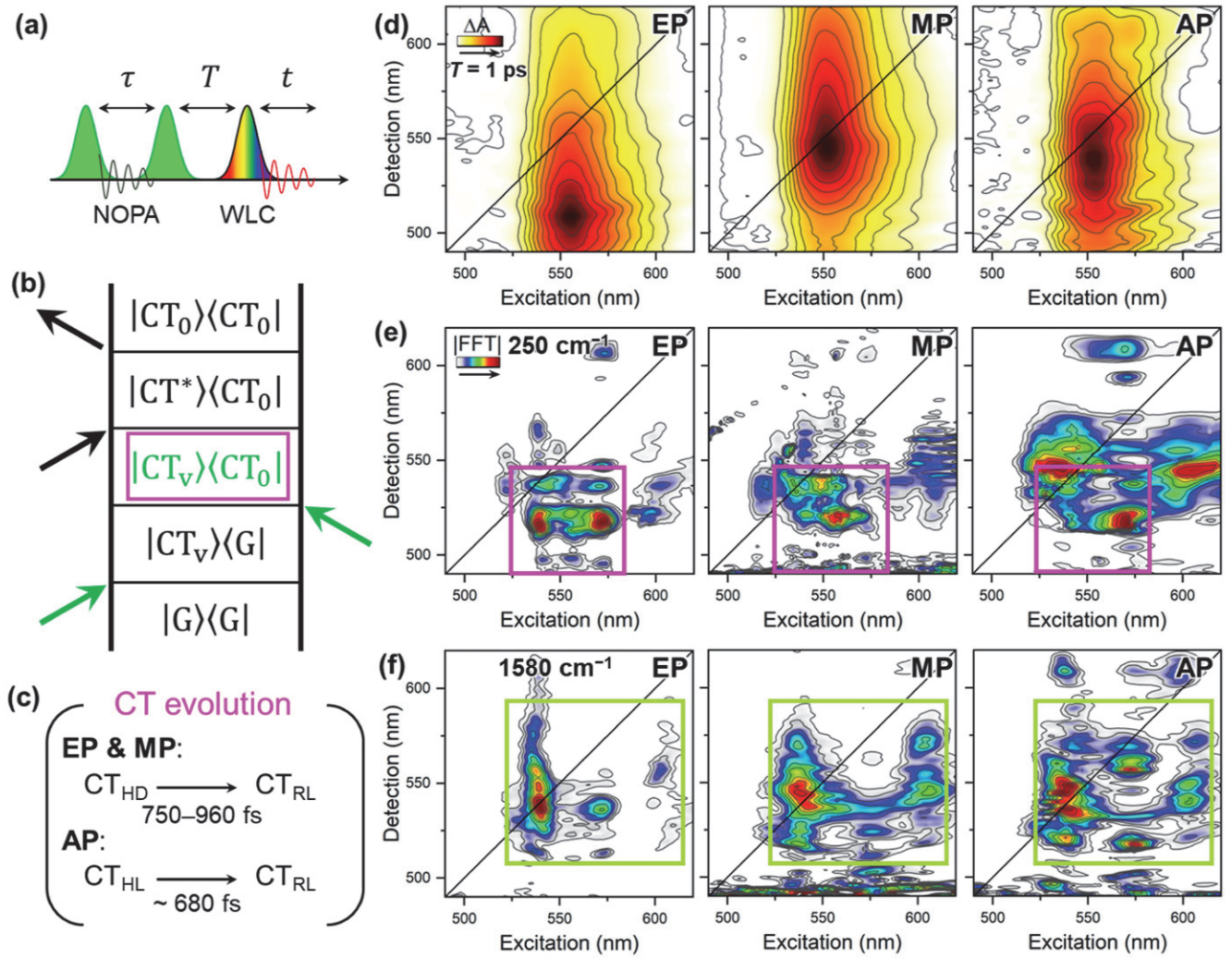


**Figure 7.** (a) Pulse train for 2DES measurements. (b) Double-sided Feynman diagram for an excited-state absorption signal pathway upon direct CT state excitation where G is the ground state and the subscripts are the vibrational quanta. (c) CT state evolution for symmetric (**EP** and **MP**) and asymmetric (**AP**) complexes where evolution times are taken from Figure 6c,d. (d) Absorptive 2DES spectra of **EP** (left), **MP** (middle), and **AP** (right) at a waiting time of 1 ps. (e) Low- (~250 $cm^{-1}$) and (f) high-frequency (~1580 $cm^{-1}$) coherence maps of **EP** (left), **MP** (middle), and **AP** (right) with highlighted regions.

and weaker $\mathbf{Per}^{+\bullet}$ absorption band around 530 nm and (2) the weaker $\mathbf{Per}^{+\bullet}$ Raman intensity (an order of magnitude) compared to those of $\mathbf{Box}^{3+\bullet}$.[38] Multiple vibrational modes were detected in a wide frequency window (150−1650 $cm^{-1}$). Among these nuclear coordinates, we focus our analysis on two regions: (1) 150−300 $cm^{-1}$, which contains low-frequency out-of-plane (oop) modes, and (2) 1500−1650 $cm^{-1}$, which contains the quadrant CC stretching modes of the $\mathbf{ExV}^{+\bullet}$ or $\mathbf{ExMeOV}^{+\bullet}$ unit.

The symmetric complexes (**EP** and **MP**) exhibit low-frequency modes at ~200 and ~250 $cm^{-1}$, whereas the asymmetric complex (**AP**) displays negligible signals in this region (Figures 6a and S21). Two representative Franck−Condon (FC) active totally symmetric vibrations in the low-frequency region are shown, where the 214 and 261 $cm^{-1}$ modes modulate the distance between the two sides, and the latter also features in-plane displacement (Figures 6b and S22). The selective appearance of these low-frequency modes is intimately related to the delocalized CT state because such collective oop vibrations are not active in the localized CT state where one of the extended viologen units is reduced and hence is direct evidence of the delocalized CT state. Thus, based on our observation that the delocalized hot CT state is initially populated in the symmetric complexes (**EP** and **MP**), there are strong correlations between the delocalized CT state and the low-frequency nuclear wavepackets, whereas the asymmetric complex (**AP**) does not show noticeable wavepacket signals. Further symmetric/asymmetric complexes will be explored for extracting general features of nuclear wavepackets from delocalized CT states. For the high-frequency region, vibrations at ~1513 and 1576 $cm^{-1}$ are marked. Notably, the mode frequencies of **EP** are slightly different, and the former mode of **EP** is relatively weaker in comparison to that of **MP** and **AP**, which confirms that the CT of **AP** is mainly composed of $\mathbf{ExMeOV}^{+\bullet} \supset \mathbf{Per}^{+\bullet}$. The quadrant CC stretching mode at 1576 $cm^{-1}$, which was calculated as 1589 $cm^{-1}$ (Figure 6b), is sensitive to the charge density;[50] thus, the CT character within the $\mathbf{ExV}^{+\bullet}$ ($\mathbf{ExMeOV}^{+\bullet}$) unit is directly reflected in the mode frequency. We note that **MP** has a slightly lower quadrant stretching frequency than **EP** because **MP** has MeO groups, which add electron density to the attached central phenylene rings.



https://doi.org/10.1021/jacs.2c13576
J. Am. Chem. Soc. 2023, 145, 8389−8400

**Charge Localization and Vibronic Decoherence of the CT States.** To explore these phenomena in the CT relaxation processes, we conducted a short-time Fourier transform (STFT) analysis on the residual time-domain signals used to obtain the FFT power spectra as shown in Figure 6c,d. The spectrograms of **EP** and **MP** in the low-frequency region highlight the fact that these collective oop vibrations dephase with time constants of less than 400 fs (Figure S23). The dephasing time constants are shorter than the localization kinetics in the BBTA results (Figure 5) as these modes broaden[26,54] the wavepackets rapidly with the various solute−solvent interactions along the charge localization coordinate. The spectrograms of the high-frequency region provide detailed information of the CT character. In the high-frequency region, **AP** also exhibits a frequency red shift even though the wavepackets evolve within the localized PES. This observation is due to the increase in CT character of the **ExMeOV**$^{+\bullet}$ unit. The mixed CT state, which is initially populated, has electron density on **Per**, while the relaxed CT state exhibits an almost negligible contribution from **Per** (Figure 3d,e). In this manner, the decoherence process from the hot ($MeO_{HL}$) to the relaxed CT state ($MeO_{RL}$) places more electron density onto the **ExMeOV**$^{2+}$ unit with a time constant of 680 fs (Figures 6d and S24). The red shift of the high-frequency mode of **AP** is directly related to the increased charge density in the **ExMeOV**$^{+\bullet}$ unit since we are monitoring its quadrant CC stretch mode, and the increased charge density decreases the force constant of the vibration. Additionally, the initially excited hot CT state ($MeO_{HL}$) shares electron density in the LUMO over both **Per** and **ExMeOV**$^{2+}$ units which then localizes into the **ExMeOV**$^{2+}$ unit ($MeO_{RL}$). For the symmetric complexes, the initial frequencies, 1604 cm$^{-1}$ (**EP**) and 1609 cm$^{-1}$ (**MP**), are higher than that of **AP** (1597 cm$^{-1}$) because each extended viologen unit in **EP** and **MP** has less electron density in the delocalized CT state. Note that the mode frequency of the **ExBox**$^{4+}$ ground state[38] is 1640 cm$^{-1}$, and as time proceeds following CT excitation, charge localization and vibronic decoherence lead to the relaxed localized state. Furthermore, because of the fact that the quadrant CC stretch mode is sensitively altered as CT relaxation takes place, this mode is an indicator of CT character and is relevant for the CT dynamics (via vibronic coupling) rather than spectator modes, while the collective low-frequency wavepackets show the existence of delocalized CT states before they relax to the localized CT state in the symmetric complexes (**EP** and **MP**).

**Two-Dimensional Electronic Spectroscopy.** The vibronic wavepackets of the CT states were also assessed by utilizing 2DES measurements. We measure 2DES signals in the pump−probe geometry with a pulse train as shown in Figure 7a, where the NOPA is used as two excitation pulses separated by coherence time ($\tau$) followed by a white-light continuum detection pulse after a waiting time ($T$). Employing 2DES here offers direct access to unique signatures of vibronic wavepackets in both the excitation and detection frequencies. Figure 7b illustrates a double-sided Feynman diagram for an excited-state absorption signal pathway, where the vibronic wavepackets of CT states in the marked state (magenta box) can propagate during $T$ based on the CT state evolution as shown in Figure 7c.

Absorptive 2DES spectra of the three complexes at a waiting time of 1 ps are displayed in Figure 7d, which only exhibit positive signals due to negligible ground-state bleaching and strong excited-CT state absorption signals in the detection window. The 2DES spectra are composed mostly of **Box**$^{3+\bullet}$ absorption signals, in accordance with the TA spectra, confirming that the **AP** signal comprises both **ExV**$^{+\bullet}$ and **ExMeOV**$^{+\bullet}$ absorption as can be seen from the excitation spectra at two different detection frequencies where the **ExBox**$^{3+\bullet}$ and **ExMeOBox**$^{3+\bullet}$ bands are located (Figure S25). The excitation spectrum of **AP** is similar to that of **EP** and **MP** at 19,700 and 18,650 cm$^{-1}$, respectively, while **ExMeOV**$^{+\bullet}$ still dominates overall signal response of **AP**. Also, there is no evidence of population transfer between **ExV**$^{+\bullet}$ and **ExMeOV**$^{+\bullet}$ due to its slow rate given the small $\Delta G$, the absence of through-space interactions, and the relatively fast CR processes. Spectral red shifts of the charged species absorption from 200 fs to 1 ps are 80, 300, and 20 cm$^{-1}$ for **EP**, **MP**, and **AP**, respectively (Figure S26). The changes in the signal ratios (Figure 5) and peak positions of the charged species absorption and the larger frequency red shift in the quadrant CC stretching mode (Figure 6d) indicate that the reorganization energy is larger for **MP** than that for **EP** during the charge localization process. As the central phenylene and adjacent pyridinium rings in the **ExV**$^{2+}$ unit can be treated as an acceptor−donor−acceptor (A−D−A) chromophore, the addition of electron-donating MeO groups in the **ExMeOV**$^{2+}$ unit (Figure 3a) increases its quadrupolar nature and $\pi$-conjugation. Thus, the greater quadrupolar character could be an important factor for enhancing charge delocalization with the guest chromophore in the CT state.

**Coherence Maps of CT States.** The vibronic wavepackets of the CT states are found in the charged species absorption and exhibit characteristic features in coherence maps (Figure 7e,f) based on the system-dependent CT evolution (Figure 7b,c). The 250 cm$^{-1}$ low-frequency mode displays similar structured coherence maps for the symmetric complexes, i.e., **EP** and **MP**, and the oscillatory signals are mostly centered in the lower diagonal region whereas those of **AP** expand more broadly and are distributed over a larger region with distinct positions. The centrally structured coherence maps of the 250 cm$^{-1}$ mode in the symmetric complexes imply that the delocalized CT states are populated through a relatively narrow excitation range compared to broad hot CT excitation. Because the complexes can have a range of superstructures in solution, the coherence signals of the delocalized CT state should feature a narrower response, and these localized signals of **EP** and **MP** along the excitation axis for the delocalized CT band should be an important indicator. In other words, the coherence maps of 250 cm$^{-1}$ of **EP** and **MP** are direct evidence of the delocalized CT state ($Ex_{HD}$ and $MeO_{HD}$). This type of collective low-frequency vibration is important for vibronic coupling[26,55−57] and structural information.[46,58,59] We note that the ∼200 cm$^{-1}$ mode may not constitute a similar case because the region seems to contain multiple signals of overlapping vibrational modes (Figure S27). For the 1580 cm$^{-1}$ high-frequency quadrant CC stretching mode, coherence signals are distributed over a larger region compared to those of the 250 cm$^{-1}$ mode, where the coherence signals of **MP** and **AP** are very similar and are assigned to **ExMeOV**$^{+\bullet}$, especially the coherence signal at the excitation of ca. 610 nm. The energy spacing between main coherence signals is ca. 2100 cm$^{-1}$, which cannot be solely explained by its vibrational energy (1580 cm$^{-1}$). Thus, we can infer that there exist a range of accessible hot CT states. Since the CT state absorption spectra do not contain distinct vibronic features and this high-


https://doi.org/10.1021/jacs.2c13576
J. Am. Chem. Soc. 2023, 145, 8389−8400

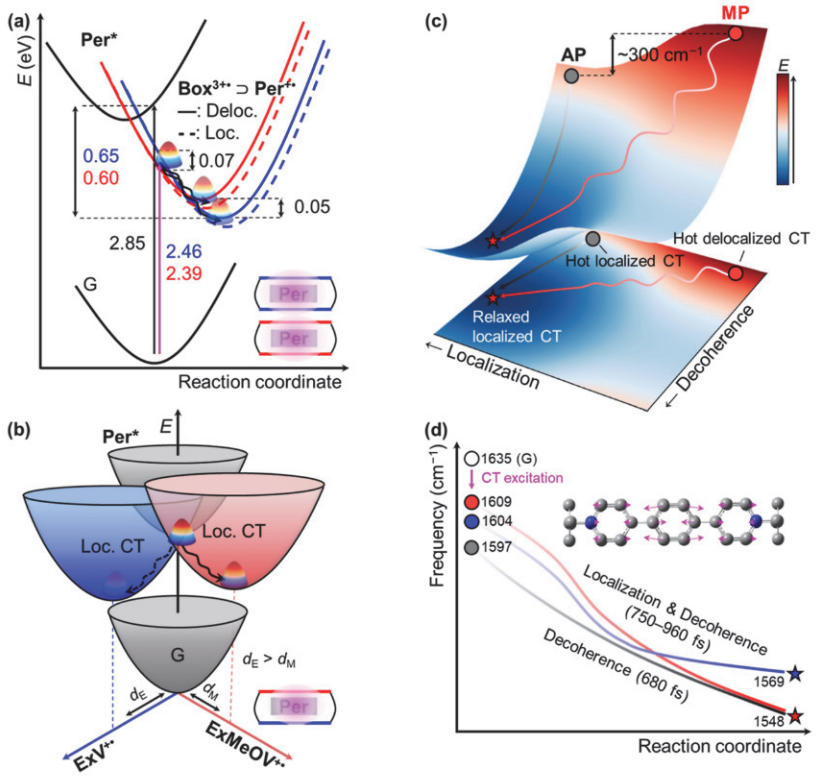


**Figure 8.** (a) PESs of symmetric **EP** (blue) and **MP** (red) complexes where PESs of delocalized (solid) and localized CT states (dashed) are separately represented. (b) PESs of the asymmetric complex (**AP**) are represented including the two localized CT states. Magnitude of displacement between the FC state (hot CT state) and the relaxed CT states is denoted $d_E$ and $d_M$ for $\mathbf{ExV}^{+\bullet}$and $\mathbf{ExMeOV}^{+\bullet}$, respectively. (c) PESs of **MP** and **AP** along the two CT relaxation coordinates (localization and decoherence), where the oscillatory features in **MP** represent the low-frequency wavepackets. The bottom 2D contour map represents projected PESs to the plane of two CT relaxation coordinates. (d) Illustrated frequency shifts of the quadrant CC stretching as the CT reaction proceeds based on the STFT results.

frequency coordinate is active in both the delocalized and localized CT states ($MeO_{HD}$ and $MeO_{HL}$), these broad features should originate from various structure-dependent coherence signals. Thus, these results imply that the $\mathbf{ExMeOV}^{+\bullet}$ unit has a broader range of hot CT states that can be excited with the NOPA.

**Potential Energy Surfaces.** Based on our experimental and computational results, we depict the energy landscape of **EP**, **MP**, and **AP** in terms of PESs and the CT relaxation pathways. Analogous to the diabatic PES (Figure 2d), we present a set of diabatic PESs for these complexes (Figure 8a,b). The energetics of these systems is summarized in Table S1. Upon photoexcitation of LE-like states, delocalized CT states ($Ex_{HD}$ and $MeO_{HD}$) are readily populated for symmetric complexes. Subsequent CT relaxation pathways are investigated through CT state excitation experiments. Both symmetric complexes, **EP** and **MP**, undergo relaxation to the localized CT states, whereas the asymmetric complex, **AP**, only relaxes within the PES of the localized CT state selectively through the $\mathbf{ExMeOV}^{2+}$ unit due to the favorable CT interactions between it and the **Per** guest. The localization could be a consequence of the dephasing of the vibronic coherences. This result is analogous to high-lying state-induced proton-coupled electron transfer,[60] intersystem crossing,[61] and intermolecular conical intersections,[62] as **AP** is confined within the $\mathbf{ExMeOV}^{2+}$ unit by the mixed hot CT state. Also, solvent−solute interactions can be larger for the $\mathbf{ExV}^{2+}$ unit because it has more freedom for structural relaxation resulting in less steric hindrance on the central rings and hence larger solute−solvent interactions. In this regard, the magnitudes of displacement ($d$) from the FC to the relaxed, localized CT state are depicted as being larger for the $\mathbf{ExV}^{2+}$ unit. Moreover, the PESs of **MP** and **AP** are compared along the two CT relaxation coordinates, which are the localization and the decoherence (Figure 8c). Note that the PES of **EP** can be described similarly to that of **MP**. Thus, the coherent vibronic wavepackets of the delocalized CT states (FC active low-frequency vibrations) accompany the localization process in **MP** (**EP**), whereas **AP** demonstrates the faster CT relaxation with only the decoherence coordinate—from the hot ($MeO_{HL}$) to the relaxed CT state ($MeO_{RL}$). We also note that the energy of this low-frequency mode (~250 $cm^{-1}$) almost coincides with the energy difference (~300 $cm^{-1}$) between hot CT states of **MP** ($MeO_{HD}$) and **AP** ($MeO_{HL}$). On the contrary, the high-frequency quadrant CC stretching mode, which is sensitive to the charge density of the $\mathbf{ExMeOV}^{2+}$ unit, exhibits frequency red shifts as the CT relaxations proceed (Figure 8d). While a torsional relaxation contributes[38] slightly to the mode frequency shift in the opposite direction (<2 $cm^{-1}$) with ~5 ps, the two relaxations, the localization and the decoherence, primarily alter the CT character before the slower structural relaxation. This work hence demonstrates that ultrafast symmetry-breaking charge separation of A−D−A (or D−A−D) complexes may be intimately related to the coupling between the low- and high-frequency vibrations and the dephasing of the vibronic coherences.


https://doi.org/10.1021/jacs.2c13576
J. Am. Chem. Soc. 2023, 145, 8389−8400

## CONCLUSIONS

We have investigated the CT reaction and subsequent relaxation pathways in the three molecular host−guest complexes where two complexes (**EP** and **MP**) are composed of symmetric hosts, and the other complex (**AP**) comprises a newly designed and synthesized asymmetric tetracationic cyclophane containing both $\mathbf{ExV}^{2+}$ and $\mathbf{ExMeOV}^{2+}$ units at each side. The direct CT process in **AP** shows that the energetically unfavorable $\mathbf{ExMeOV}^{2+}$ unit is reduced rather than the more facile $\mathbf{ExV}^{2+}$ unit due to stronger orbital overlap with **Per** owing to structural restrictions imposed by the 2,5-dimethoxy substituents, which ultimately facilitates the CT interaction between the **Per** guest and the $\mathbf{ExMeOV}^{2+}$ unit. We have shown how the coherent vibronic wavepackets can be used to detect the charge-delocalized CT state and probe the evolution of the CT character in terms of charge localization and vibronic decoherence. In particular, the low-frequency collective vibrational modes of the host, which decohere rapidly, are the direct indicator of the delocalized CT states because these modes were only detected for the symmetric complexes and showed characteristic coherence maps with the localized features along the excitation axis. The high-frequency quadrant CC stretching mode is highly sensitive to the nature and degree of CT character. Because the frequency red shift in **AP** is solely due to the decoherence coordinate, the delocalization effect of symmetric complexes (**EP** and **MP**) is also revealed by the frequency shift. Therefore, we have provided fundamental design principles for non-covalent A−D−A quadrupolar systems, where a subtle modification to the host can direct charge flow to one of the acceptors when it induces a stronger CT interaction between the donor and acceptor. We also have provided experimental evidence of a delocalized intermediate in the symmetric complexes encompassing both acceptors and the donor and that the symmetry-breaking process is accompanied by the dephasing of collective nuclear motions.

## ASSOCIATED CONTENT

### Supporting Information

The Supporting Information is available free of charge at https://pubs.acs.org/doi/10.1021/jacs.2c13576.

Synthetic details, experimental details including NMR titrations, X-ray crystal data, electrochemical characterizations, steady-state absorption and emission, narrowband/BBTA and 2DES measurements, computational details, and crystallographic data for $\mathbf{ExMeOVBox}^{4+}$, $\mathbf{ExMeOBox}^{4+} \supset \mathbf{Per}$, and $\mathbf{ExMeOVBox}^{4+} \supset \mathbf{Per}$ (PDF)

### Accession Codes

CCDC 2170005 and 2226097−2226098 contain the supplementary crystallographic data for this paper. These data can be obtained free of charge via www.ccdc.cam.ac.uk/data_request/cif, or by emailing data_request@ccdc.cam.ac.uk, or by contacting The Cambridge Crystallographic Data Centre, 12 Union Road, Cambridge CB2 1EZ, UK; fax: +44 1223 336033.

## AUTHOR INFORMATION


### Corresponding Authors

**J. Fraser Stoddart** − *Department of Chemistry, Northwestern University, Evanston, Illinois 60208-3113, United States; Stoddart Institute of Molecular Science, Department of Chemistry, Zhejiang University, Hangzhou 310027, China; ZJU-Hangzhou Global Scientific and Technological Innovation Center, Hangzhou 311215, China; School of Chemistry, University of New South Wales, Sydney, New South Wales 2052, Australia;* orcid.org/0000-0003-3161-3697; Email: stoddart@northwestern.edu

**Ryan M. Young** − *Department of Chemistry and Institute for Sustainability and Energy at Northwestern, Northwestern University, Evanston, Illinois 60208-3113, United States;* orcid.org/0000-0002-5108-0261; Email: ryan.young@northwestern.edu

**Michael R. Wasielewski** − *Department of Chemistry and Institute for Sustainability and Energy at Northwestern, Northwestern University, Evanston, Illinois 60208-3113, United States;* orcid.org/0000-0003-2920-5440; Email: m-wasielewski@northwestern.edu

### Authors

**Taeyeon Kim** − *Department of Chemistry and Institute for Sustainability and Energy at Northwestern, Northwestern University, Evanston, Illinois 60208-3113, United States;* orcid.org/0000-0003-0408-9498

**Yuanning Feng** − *Department of Chemistry, Northwestern University, Evanston, Illinois 60208-3113, United States;* Present Address: Department of Chemistry, Sungkyunkwan University, Suwon 16419, Republic of Korea; orcid.org/0000-0002-8832-0767

**James P. O'Connor** − *Department of Chemistry and Institute for Sustainability and Energy at Northwestern, Northwestern University, Evanston, Illinois 60208-3113, United States;* orcid.org/0000-0002-8586-9842

Complete contact information is available at: https://pubs.acs.org/10.1021/jacs.2c13576

### Author Contributions

[⊥]T.K. and Y.F. contributed equally to this work.


### Notes

The authors declare no competing financial interest.

## ACKNOWLEDGMENTS

This work was supported by the National Science Foundation under award no. DMR-2003739 (M.R.W. and R.M.Y.) and Northwestern University (J.F.S.). This work made use of the IMSERC MS and NMR facility at Northwestern University, which has received support from the Soft and Hybrid Nanotechnology Experimental (SHyNE) Resource (NSF ECCS-2025633), the State of Illinois, the International Institute for Nanotechnology (IIN), and Northwestern University.

## REFERENCES

(1) Romero, E.; Novoderezhkin, V. I.; Van Grondelle, R. Quantum design of photosynthesis for bio-inspired solar-energy conversion. *Nature* **2017**, *543*, 355−365.

(2) Niedringhaus, A.; Policht, V. R.; Sechrist, R.; Konar, A.; Laible, P. D.; Bocian, D. F.; Holten, D.; Kirmaier, C.; Ogilvie, J. P. Primary processes in the bacterial reaction center probed by two-dimensional electronic spectroscopy. *Proc. Natl. Acad. Sci. U.S.A.* **2018**, *115*, 3563−3568.

(3) Ponseca, C. S., Jr.; Chabera, P.; Uhlig, J.; Persson, P.; Sundstrom, V. Ultrafast electron dynamics in solar energy conversion. *Chem. Rev.* **2017**, *117*, 10940−11024.

(4) Lian, S.; Kodaimati, M. S.; Dolzhnikov, D. S.; Calzada, R.; Weiss, E. A. Powering a $CO_2$ reduction catalyst with visible light through multiple sub-picosecond electron transfers from a quantum dot. *J. Am. Chem. Soc.* **2017**, *139*, 8931−8938.

(5) Chang, W.; Congreve, D. N.; Hontz, E.; Bahlke, M. E.; McMahon, D. P.; Reineke, S.; Wu, T. C.; Bulović, V.; Van Voorhis, T.; Baldo, M. A. Spin-dependent charge transfer state design rules in organic photovoltaics. *Nat. Commun.* **2015**, *6*, 6415.
(6) Inganas, O. Organic photovoltaics over three decades. *Adv. Mater.* **2018**, *30*, No. e1800388.
(7) Jakowetz, A. C.; Bohm, M. L.; Zhang, J.; Sadhanala, A.; Huettner, S.; Bakulin, A. A.; Rao, A.; Friend, R. H. What controls the rate of ultrafast charge transfer and charge separation efficiency in organic photovoltaic blends. *J. Am. Chem. Soc.* **2016**, *138*, 11672−11679.
(8) Liu, F.; Zhou, L.; Liu, W.; Zhou, Z.; Yue, Q.; Zheng, W.; Sun, R.; Liu, W.; Xu, S.; Fan, H.; Feng, L.; Yi, Y.; Zhang, W.; Zhu, X. Organic solar cells with 18% efficiency enabled by an alloy acceptor: A two-in-one strategy. *Adv. Mater.* **2021**, *33*, No. e2100830.
(9) Karki, A.; Gillett, A. J.; Friend, R. H.; Nguyen, T. Q. The path to 20% power conversion efficiencies in nonfullerene acceptor organic solar cells. *J. Mater. Chem. C* **2020**, *11*, 202003441.
(10) Zhu, L.; Zhang, M.; Xu, J.; Li, C.; Yan, J.; Zhou, G.; Zhong, W.; Hao, T.; Song, J.; Xue, X.; Zhou, Z.; Zeng, R.; Zhu, H.; Chen, C. C.; MacKenzie, R. C. I.; Zou, Y.; Nelson, J.; Zhang, Y.; Sun, Y.; Liu, F. Single-junction organic solar cells with over 19% efficiency enabled by a refined double-fibril network morphology. *Nat. Mater.* **2022**, *21*, 656−663.
(11) Bakulin, A. A.; Rao, A.; Pavelyev, V. G.; van Loosdrecht, P. H. M.; Pshenichnikov, M. S.; Niedzialek, D.; Cornil, J.; Beljonne, D.; Friend, R. H. The role of driving energy and delocalized states for charge separation in organic semiconductors. *Science* **2012**, *335*, 1340−1344.
(12) Banerji, N. Sub-picosecond delocalization in the excited state of conjugated homopolymers and donor−acceptor copolymers. *J. Mater. Chem. C* **2013**, *1*, 3052.
(13) Tamura, H.; Burghardt, I. Ultrafast charge separation in organic photovoltaics enhanced by charge delocalization and vibronically hot exciton dissociation. *J. Am. Chem. Soc.* **2013**, *135*, 16364−16367.
(14) Ghosh, R.; Pochas, C. M.; Spano, F. C. Polaron delocalization in conjugated polymer films. *J. Phys. Chem. C* **2016**, *120*, 11394−11406.
(15) Zhang, G.; Chen, X. K.; Xiao, J.; Chow, P. C. Y.; Ren, M.; Kupgan, G.; Jiao, X.; Chan, C. C. S.; Du, X.; Xia, R.; Chen, Z.; Yuan, J.; Zhang, Y.; Zhang, S.; Liu, Y.; Zou, Y.; Yan, H.; Wong, K. S.; Coropceanu, V.; Li, N.; Brabec, C. J.; Bredas, J. L.; Yip, H. L.; Cao, Y. Delocalization of exciton and electron wavefunction in non-fullerene acceptor molecules enables efficient organic solar cells. *Nat. Commun.* **2020**, *11*, 3943.
(16) Falke, S. M.; Rozzi, C. A.; Brida, D.; Maiuri, M.; Amato, M.; Sommer, E.; De Sio, A.; Rubio, A.; Cerullo, G.; Molinari, E.; et al. Coherent ultrafast charge transfer in an organic photovoltaic blend. *Science* **2014**, *344*, 1001−1005.
(17) De Sio, A.; Lienau, C. Vibronic coupling in organic semiconductors for photovoltaics. *Phys. Chem. Chem. Phys.* **2017**, *19*, 18813−18830.
(18) Balzer, D.; Kassal, I. Even a little delocalization produces large kinetic enhancements of charge-separation efficiency in organic photovoltaics. *Sci. Adv.* **2022**, *8*, No. eabl9692.
(19) Delor, M.; Sazanovich, I. V.; Towrie, M.; Weinstein, J. A. Probing and exploiting the interplay between nuclear and electronic motion in charge transfer processes. *Acc. Chem. Res.* **2015**, *48*, 1131−1139.
(20) Dereka, B.; Koch, M.; Vauthey, E. Looking at photoinduced charge transfer processes in the IR: Answers to several long-standing questions. *Acc. Chem. Res.* **2017**, *50*, 426−434.
(21) Kim, T.; Kim, J.; Mori, H.; Park, S.; Lim, M.; Osuka, A.; Kim, D. Symmetry-breaking charge transfer in the excited state of directly linked push-pull porphyrin arrays. *Phys. Chem. Chem. Phys.* **2017**, *19*, 13970−13977.
(22) Cho, M. Coherent two-dimensional optical spectroscopy. *Chem. Rev.* **2008**, *108*, 1331−1418.
(23) Dean, J. C.; Scholes, G. D. Coherence spectroscopy in the condensed phase: Insights into molecular structure, environment, and interactions. *Acc. Chem. Res.* **2017**, *50*, 2746−2755.
(24) Biswas, S.; Kim, J.; Zhang, X.; Scholes, G. D. Coherent two-dimensional and broadband electronic spectroscopies. *Chem. Rev.* **2022**, *122*, 4257−4321.
(25) Lin, C.; Kim, T.; Schultz, J. D.; Young, R. M.; Wasielewski, M. R. Accelerating symmetry-breaking charge separation in a perylenediimide trimer through a vibronically coherent dimer intermediate. *Nat. Chem.* **2022**, *14*, 786−793.
(26) Kim, T.; Lin, C.; Schultz, J. D.; Young, R. M.; Wasielewski, M. R. $\pi$-Stacking-dependent vibronic couplings drive excited-state dynamics in perylenediimide assemblies. *J. Am. Chem. Soc.* **2022**, *144*, 11386−11396.
(27) Zhang, T.; Gasparini, N. Ternary organic solar cells: Insights into charge and energy transfer processes. *Appl. Phys. Lett.* **2022**, *120*, 250501.
(28) Xu, X.; Li, Y.; Peng, Q. Ternary blend organic solar cells: Understanding the morphology from recent progress. *Adv. Mater.* **2022**, *34*, No. e2107476.
(29) Gasparini, N.; Salleo, A.; McCulloch, I.; Baran, D. The role of the third component in ternary organic solar cells. *Nat. Rev. Mater.* **2019**, *4*, 229−242.
(30) Gao, W.; Qi, F.; Peng, Z.; Lin, F. R.; Jiang, K.; Zhong, C.; Kaminsky, W.; Guan, Z.; Lee, C. S.; Marks, T. J.; Ade, H.; Jen, A. K. Achieving 19% power conversion efficiency in planar-mixed heterojunction organic solar cells using a pseudosymmetric electron acceptor. *Adv. Mater.* **2022**, *34*, No. e2202089.
(31) Barnes, J. C.; Juricek, M.; Strutt, N. L.; Frasconi, M.; Sampath, S.; Giesener, M. A.; McGrier, P. L.; Bruns, C. J.; Stern, C. L.; Sarjeant, A. A.; Stoddart, J. F. Exbox: A polycyclic aromatic hydrocarbon scavenger. *J. Am. Chem. Soc.* **2013**, *135*, 183−192.
(32) Feng, Y.; Das, P. J.; Young, R. M.; Brown, P. J.; Hornick, J. E.; Weber, J. A.; Seale, J. S. W.; Stern, C. L.; Wasielewski, M. R.; Stoddart, J. F. Alkoxy-substituted quadrupolar fluorescent dyes. *J. Am. Chem. Soc.* **2022**, *144*, 16841−16854.
(33) Thordarson, P. Determining association constants from titration experiments in supramolecular chemistry. *Chem. Soc. Rev.* **2011**, *40*, 1305−1323.
(34) Wu, Y. L.; Zhou, J. W.; Nelson, J. N.; Young, R. M.; Krzyaniak, M. D.; Wasielewski, M. R. Covalent radical pairs as spin qubits: Influence of rapid electron motion between two equivalent sites on spin coherence. *J. Am. Chem. Soc.* **2018**, *140*, 13011−13021.
(35) Chen, X. K.; Coropceanu, V.; Bredas, J. L. Assessing the nature of the charge-transfer electronic states in organic solar cells. *Nat. Commun.* **2018**, *9*, 5295.
(36) Coropceanu, V.; Chen, X. K.; Wang, T. H.; Zheng, Z. L.; Bredas, J. L. Charge-transfer electronic states in organic solar cells. *Nat. Rev. Mater.* **2019**, *4*, 689−707.
(37) Brunschwig, B. S.; Creutz, C.; Sutin, N. Optical transitions of symmetrical mixed-valence systems in the Class II−III transition regimeElectronic supplementary information (ESI) is available: derivation of eqn. (39c), table summarizing the relationships between band maxima and band widths predicted by the two-state model and table of spectral properties of mixed-valence ruthenium(II)/(III) bridged by pyrazine and dicyanamide. See http://www.rsc.org/suppdata/cs/b0/b008034i/. *Chem. Soc. Rev.* **2002**, *31*, 168−184.
(38) Young, R. M.; Dyar, S. M.; Barnes, J. C.; Juricek, M.; Stoddart, J. F.; Co, D. T.; Wasielewski, M. R. Ultrafast conformational dynamics of electron transfer in Exbox$^{4+}$⊂perylene. *J. Phys. Chem. A* **2013**, *117*, 12438−12448.
(39) Zhou, J.; Wu, Y.; Roy, I.; Samanta, A.; Stoddart, J. F.; Young, R. M.; Wasielewski, M. R. Choosing sides: Unusual ultrafast charge transfer pathways in an asymmetric electron-accepting cyclophane that binds an electron donor. *Chem. Sci.* **2019**, *10*, 4282−4292.
(40) Marcus, R. A. On the theory of oxidation-reduction reactions involving electron transfer. I. *J. Chem. Phys.* **1956**, *24*, 966−978.


https://doi.org/10.1021/jacs.2c13576
J. Am. Chem. Soc. 2023, 145, 8389−8400

(41) Marcus, R. A. On the theory of electron-transfer reactions. VI. Unified treatment for homogeneous and electrode reactions. *J. Chem. Phys.* **1965**, *43*, 679−701.
(42) Wu, Y.; Young, R. M.; Frasconi, M.; Schneebeli, S. T.; Spenst, P.; Gardner, D. M.; Brown, K. E.; Würthner, F.; Stoddart, J. F.; Wasielewski, M. R. Ultrafast photoinduced symmetry-breaking charge separation and electron sharing in perylenediimide molecular triangles. *J. Am. Chem. Soc.* **2015**, *137*, 13236−13239.
(43) Kang, S.; Kim, T.; Hong, Y.; Würthner, F.; Kim, D. Charge-delocalized state and coherent vibrational dynamics in rigid PBI H-aggregates. *J. Am. Chem. Soc.* **2021**, *143*, 9825−9833.
(44) Szakács, Z.; Vauthey, E. Excited-state symmetry breaking and the Laporte rule. *J. Phys. Chem. Lett.* **2021**, *12*, 4067−4071.
(45) Tempelaar, R.; Spano, F. C.; Knoester, J.; Jansen, T. L. C. Mapping the evolution of spatial exciton coherence through time-resolved fluorescence. *J. Phys. Chem. Lett.* **2014**, *5*, 1505−1510.
(46) Kim, T.; Kang, S.; Kirchner, E.; Bialas, D.; Kim, W.; Würthner, F.; Kim, D. Switching resonance character within merocyanine stacks and its impact on excited-state dynamics. *Chem* **2021**, *7*, 715−725.
(47) Hoffman, D. P.; Ellis, S. R.; Mathies, R. A. Characterization of a conical intersection in a charge-transfer dimer with two-dimensional time-resolved stimulated Raman spectroscopy. *J. Phys. Chem. A* **2014**, *118*, 4955−4965.
(48) Dereka, B.; Rosspeintner, A.; Li, Z.; Liska, R.; Vauthey, E. Direct visualization of excited-state symmetry breaking using ultrafast time-resolved infrared spectroscopy. *J. Am. Chem. Soc.* **2016**, *138*, 4643−4649.
(49) Kim, T.; Kim, W.; Vakuliuk, O.; Gryko, D. T.; Kim, D. Two-step charge separation passing through the partial charge-transfer state in a molecular dyad. *J. Am. Chem. Soc.* **2020**, *142*, 1564−1573.
(50) Kim, W.; Kim, T.; Kang, S.; Hong, Y.; Würthner, F.; Kim, D. Tracking structural evolution during symmetry-breaking charge separation in quadrupolar perylene bisimide with time-resolved impulsive stimulated Raman spectroscopy. *Angew. Chem., Int. Ed.* **2020**, *59*, 8571−8578.
(51) Donohoo-Vallett, P. J.; Bragg, A. E. $\pi$-Delocalization and the vibrational spectroscopy of conjugated materials: Computational insights on Raman frequency dispersion in thiophene, furan, and pyrrole oligomers. *J. Phys. Chem. B* **2015**, *119*, 3583−3594.
(52) Sung, J.; Kim, P.; Fimmel, B.; Würthner, F.; Kim, D. Direct observation of ultrafast coherent exciton dynamics in helical $\pi$-stacks of self-assembled perylene bisimides. *Nat. Commun.* **2015**, *6*, 8646.
(53) Kim, W.; Tahara, S.; Kuramochi, H.; Takeuchi, S.; Kim, T.; Tahara, T.; Kim, D. Mode-specific vibrational analysis of exciton delocalization and structural dynamics in conjugated oligomers. *Angew. Chem., Int. Ed.* **2021**, *60*, 16999−17008.
(54) Rafiq, S.; Scholes, G. D. From fundamental theories to quantum coherences in electron transfer. *J. Am. Chem. Soc.* **2019**, *141*, 708−722.
(55) Schultz, J. D.; Shin, J. Y.; Chen, M.; O'Connor, J. P.; Young, R. M.; Ratner, M. A.; Wasielewski, M. R. Influence of vibronic coupling on ultrafast singlet fission in a linear terrylenediimide dimer. *J. Am. Chem. Soc.* **2021**, *143*, 2049−2058.
(56) Arsenault, E. A.; Yoneda, Y.; Iwai, M.; Niyogi, K. K.; Fleming, G. R. Vibronic mixing enables ultrafast energy flow in light-harvesting complex II. *Nat. Commun.* **2020**, *11*, 1460.
(57) Gaynor, J. D.; Sandwisch, J.; Khalil, M. Vibronic coherence evolution in multidimensional ultrafast photochemical processes. *Nat. Commun.* **2019**, *10*, 5621.
(58) Gil-Santos, E.; Ruz, J. J.; Malvar, O.; Favero, I.; Lemaitre, A.; Kosaka, P. M.; Garcia-Lopez, S.; Calleja, M.; Tamayo, J. Optomechanical detection of vibration modes of a single bacterium. *Nat. Nanotechnol.* **2020**, *15*, 469−474.
(59) Paulus, B. C.; Adelman, S. L.; Jamula, L. L.; McCusker, J. K. Leveraging excited-state coherence for synthetic control of ultrafast dynamics. *Nature* **2020**, *582*, 214−218.
(60) Corp, K. L.; Rabe, E. J.; Huang, X.; Ehrmaier, J.; Kaiser, M. E.; Sobolewski, A. L.; Domcke, W.; Schlenker, C. W. Control of excited-state proton-coupled electron transfer by ultrafast pump-push-probe spectroscopy in heptazine-phenol complexes: Implications for photochemical water oxidation. *J. Phys. Chem. C* **2020**, *124*, 9151−9160.
(61) Beldjoudi, Y.; Atilgan, A.; Weber, J. A.; Roy, I.; Young, R. M.; Yu, J.; Deria, P.; Enciso, A. E.; Wasielewski, M. R.; Hupp, J. T.; Stoddart, J. F. Supramolecular porous organic nanocomposites for heterogeneous photocatalysis of a sulfur mustard simulant. *Adv. Mater.* **2020**, *32*, No. e2001592.
(62) De Sio, A.; Sommer, E.; Nguyen, X. T.; Groß, L.; Popovic, D.; Nebgen, B. T.; Fernandez-Alberti, S.; Pittalis, S.; Rozzi, C. A.; Molinari, E.; Mena-Osteritz, E.; Bauerle, P.; Frauenheim, T.; Tretiak, S.; Lienau, C. Intermolecular conical intersections in molecular aggregates. *Nat. Nanotechnol.* **2021**, *16*, 63−68.




https://doi.org/10.1021/jacs.2c13576
*J. Am. Chem. Soc.* 2023, 145, 8389−8400